

# Electronic, Mechanical, Vibrational and Piezoelectric Properties of $\text{Mg}_3\text{X}_2$ ( $\text{X} = \text{As}, \text{Sb}$ ) Monolayers

G.-X. YIN, K.-T. WANG AND H.-L. CUI\*

*School of Physics and Engineering, Henan University of Science and Technology, 263 Kaiyuan Avenue, Luoyang 471023, China*

Received: 01.03.2024 & Accepted: 17.06.2024

Doi: [10.12693/APhysPolA.146.186](https://doi.org/10.12693/APhysPolA.146.186)

\*e-mail: [lzl114077@sina.com](mailto:lzl114077@sina.com)

Recently, bulk  $\text{Mg}_3\text{X}_2$  ( $\text{X}=\text{As}, \text{Sb}$ ) have been intensively studied for their unique properties for thermoelectric use. However, studies on their two-dimensional counterparts are not sufficient. In this work, we systematically investigated the electronic, mechanical, vibrational, and piezoelectric properties of  $\text{Mg}_3\text{X}_2$  ( $\text{X} = \text{As}, \text{Sb}$ ) monolayers. The results indicate that both monolayers have negative formation energies with dynamical and mechanical stability.  $\text{Mg}_3\text{As}_2$  monolayer is a narrow band gap semiconductor, while  $\text{Mg}_3\text{Sb}_2$  monolayer is an indirect one. The origin of the band structure was revealed by the calculated partial density of states. The bonding property of both monolayers was analyzed by different methods. Elastic constants were obtained by density functional perturbation theory, and the related physical quantities were derived and analyzed. In-plane strengths along the zigzag and armchair directions of both materials were calculated, and the fracture mechanisms were uncovered. The vibrational modes at the Brillouin center were classified through group theory analysis, and the corresponding eigenvectors and frequencies were calculated and presented. Infrared vibrational spectra were simulated, and the reason for the vanishment of some infrared peaks was disclosed. Piezoelectric and dielectric coefficients were also computed and discussed.

topics: electronic property, mechanical property, vibrational property, piezoelectric property

## 1. Introduction

Bulk  $\text{Mg}_3\text{X}_2$  ( $\text{X} = \text{As}, \text{Sb}$ ) are narrow band gap semiconductors with low thermal conductivity. They are also interesting because their stable phases have melting points higher than their constituent simple substances [1].  $\text{Mg}_3\text{As}_2$  crystallizes in a cubic  $\text{Mn}_2\text{O}_3$ -type structure below 1000 K, which becomes a trigonal  $\text{La}_2\text{O}_3$ -type phase beyond 1100 K [2]. The experimentally reported band gap of  $\text{Mg}_3\text{As}_2$  is 2.2 eV [3]. It was found that the cubic phase transits to a new one with a space group of  $C2/m$  at about 12 GPa, which further changes to a phase with  $P-1$  symmetry at around 30 GPa. All of them are narrow band gap semiconductors with theoretical values no larger than 2.1 eV [4].  $\text{Mg}_3\text{Sb}_2$  has a trigonal  $\text{La}_2\text{O}_3$ -type structure with an experimental band gap of 0.82 eV at ambient conditions [5]. Studies on phase transition under high pressure indicate that  $\text{Mg}_3\text{Sb}_2$  has a  $C_m$  phase at 5 GPa and a  $C2/m$  phase at 12.7 GPa, both with a metallic characteristics [6]. Calderón-Cueva et al. [7] studied the structural and bonding properties of  $\text{Mg}_3\text{Sb}_2$  under pressure up to 50 GPa by synchrotron X-ray diffraction, which reveals that the octahedral Mg–Sb bonds are more prone to be compressed than the tetrahedral ones, confirming

the conjecture that the former play a very important role in deciding the anomalous thermal property of  $\text{Mg}_3\text{Sb}_2$ .

The unique properties of  $\text{Mg}_3\text{X}_2$ , especially  $\text{Mg}_3\text{Sb}_2$ , make them easy to modulate for thermoelectric applications [8]. As an experiment, Condrón et al. [9] synthesized  $\text{Mg}_3\text{Sb}_2$  by different methods and characterized its microstructure. Measurable oxygen content at the grain boundary was found, and a low thermoelectric figure of merit (ZT) of about 0.2 at 875 K was obtained. To improve the ZT value, Bhardwaj et al. [10] doped  $\text{Mg}_3\text{Sb}_2$  with Bi by spark plasma sintering, characterized them by X-ray diffraction and high-resolution transmission electron microscopy, and studied their power factor and thermal conductivity. They found that doping 0.2 at% Bi to replace Sb can enhance the ZT to 0.6 at 750 K. Ren et al. [11] co-doped  $\text{Mg}_3\text{Sb}_2$  with Na and Zn by ball milling and hot pressing. The results show that co-doping can significantly enhance the hole mobility and reduce lattice thermal conductivity, which greatly increases both the power factor and ZT, leading to the largest ZT of 0.8 at 773 K. Liu et al. [12] optimized the electronic properties of n-type  $\text{Mg}_{3.2}\text{Bi}_{1.5}\text{Sb}_{0.5}$  by delicate microstructural design to remove the thermal resistance originating from grain boundary and obtained a high ZT — above 1 in the temperature range of 323–423 K.

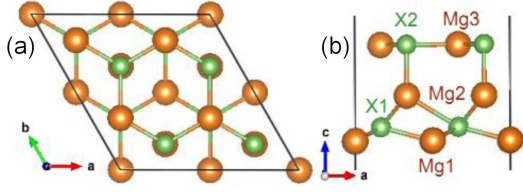


Fig. 1. Crystal structure of  $\text{Mg}_3\text{X}_2$  ( $\text{X} = \text{As}, \text{Sb}$ ) monolayers in a  $2 \times 2$  supercell: (a) top view and (b) side view.

In terms of theoretical research, Xu et al. [13] studied the electronic and thermoelectric properties of  $\text{Mg}_3\text{Sb}_2$  and discovered that the absolute Seebeck coefficient of n-type doping is higher than that of p-type doping due to the larger band degeneracy at the conduction band minimum. Li et al. [14] also investigated the band structure and thermoelectric properties of n-type  $\text{Mg}_3\text{Sb}_2$  through the first-principles method, which obtained a great ZT of 3.1 at 725 K with the lowest lattice thermal conductivity and an optimized carrier concentration. Sun et al. [15] theoretically demonstrated that replacing the Mg atoms at the octahedral positions with more ionic dopants can notably boost the band degeneracy of the conduction band minimum of  $\text{Mg}_3\text{Sb}_2$ , lower lattice thermal conductivity and increase Seebeck coefficients and power factors. Through studying the band structure, effective mass and Fermi surface of n-type  $\text{Mg}_3\text{Sb}_{2-x}\text{Bi}_x$  ( $x = 0, 1, 2$ ), Zhang and Iversen [16] found that n-type  $\text{Mg}_3\text{SbBi}$  has a greater power factor and a lower optimized carrier concentration than n-type  $\text{Mg}_3\text{Sb}_2$  at 300 K. Xia et al. [17] studied the pressure effect on the thermoelectric properties of n-type and p-type  $\text{Mg}_3\text{Sb}_2$  and discovered that they both have enhanced power factors under pressure with different mechanism. In n-type, the enhancement is caused by the increase in the effective mass near the conduction band edge, whereas in p-type, it is induced by the lowered electron scattering rate and a longer electron relaxation time originating from the suppressed electron-phonon interaction near the valence band edge. Wang et al. [18] researched the thermoelectric properties of  $\text{Mg}_3\text{X}_2$  ( $\text{X} = \text{As}$  and  $\text{X} = \text{Sb}$ ) and found that the ZTs of the n-type are 2.58 and 1.38, respectively, while of the p-type are 1.39 and 0.64. There are also some theoretical works reporting other properties of  $\text{Mg}_3\text{X}_2$  ( $\text{X} = \text{As}, \text{Sb}$ ), i.e., elastic and lattice dynamic properties [19], structural, electronic, optical, and thermoelectric properties [20], bonding properties [21], elastic properties [22], and electronic, optical, elastic, and infrared properties [23].

Theoretical study proposed the existence of  $\text{Mg}_3\text{Sb}_2$  monolayer [24], where they found that the ZT value of  $\text{Mg}_3\text{Sb}_2$  monolayer can reach 2.5, which is much higher than that of its bulk. The thermoelectric properties of  $\text{Mg}_3\text{Sb}_{2-x}\text{Bi}_x$  ( $x = 0, 1, 2$ )

monolayers were also studied by Chang et al. [25]. Enlightened by the above works, we extended the research object to the  $\text{Mg}_3\text{As}_2$  monolayer, but found by *ab initio* molecular dynamics that its thermal stability is not as high as expected. Thus, we turned to the study of electronic, mechanical, vibrational, and piezoelectric properties of  $\text{Mg}_3\text{X}_2$  ( $\text{X} = \text{As}, \text{Sb}$ ) monolayers by first-principles calculation.  $\text{Mg}_3\text{Bi}_2$  is ruled out because it has a formation energy of about zero with low thermal stability.

## 2. Computational details

In this work, the Vienna *Ab initio* Simulation Package (VASP) code [26] is used to explore the aforementioned properties of the monolayers. The Perdew–Burke–Ernzerhof (PBE) functional [27] is used to calculate the interaction energy among electrons in the processes of structural relaxation and property calculation. The projector augmented wave (PAW) pseudopotentials [28] are employed to describe the interaction energy between nuclei and electrons. The  $c$  axes of these monolayers are set to 25 Å to avoid the potential disturbance of the adjacent images. The wave function of each monolayer is unfolded by a series of plane waves with a cutoff energy of 320 eV — 1.5 times that of the maximum value recommended by VASP. Brillouin zone integration is carried out with a  $k$ -spacing of  $0.03 \text{ \AA}^{-1}$  based on the Monkhorst–Pack scheme [29]. Tests imply that the above parameters can guarantee that the total energy converges to  $10^{-6} \text{ eV/atom}$  and the force among atoms converges to  $0.01 \text{ eV/\AA}$ . Elastic and piezoelectric constants are attained through the density functional perturbation method implemented in VASP. The phonopy code [30] is utilized to gain the phonon spectra of these systems. Because the PBE functional always underestimates band gaps, we also calculated the band structures and partial densities of states (PDOS) of these monolayers using the HSE06 functional [31] based on the PBE-relaxed crystal structures, as done in references [23, 32, 33].

## 3. Results and discussion

### 3.1. Structure and stability

$\text{Mg}_3\text{X}_2$  ( $\text{X} = \text{As}, \text{Sb}$ ) monolayers are derived from their bulk counterparts [7, 34]. They have a space group of P3m1 and all atoms are nonequivalent, as shown in Fig. 1. The relaxed lattice constants of  $\text{Mg}_3\text{X}_2$  ( $\text{X} = \text{As/Sb}$ ) are  $a = b = 4.381/4.735 \text{ \AA}$ , and the Wyckoff sites of atoms are: Mg1 1a (0, 0, 0.4468/0.4449), Mg2 1c (2/3, 1/3, 0.5352/0.5356), Mg3 1b (1/3, 2/3, 0.6351/0.6298), X1 1b (1/3, 2/3, 0.4738/0.4718),

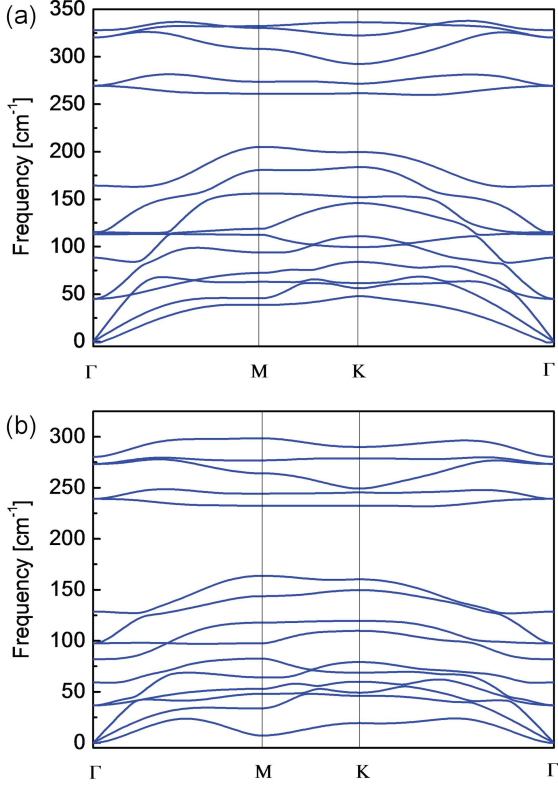


Fig. 2. Calculated phonon spectra of (a)  $\text{Mg}_3\text{As}_2$  and (b)  $\text{Mg}_3\text{Sb}_2$  monolayer.

and X2 1c (2/3, 1/3, 0.6350/0.6438). The crystal structure can be viewed as being formed by two displaced hexagonal MgX layers linked by the intercalated Mg atoms. In  $\text{Mg}_3\text{As}_2$  ( $\text{Mg}_3\text{Sb}_2$ ), each Mg1 atom bonds with three As1 (Sb1) atoms with a bond length of 2.617 (2.815) Å, each Mg2 atom is coordinated by three As1 (Sb1) atoms and one As2 (Sb2) atom with distances of 2.960 (3.166) Å and 2.496 (2.705) Å, respectively, and each Mg3 atom is surrounded by three As2 (Sb2) atoms with a bond length of 2.529 (2.756) Å.

Cohesive energy measures the energy released when isolated atoms form a crystal, which can be computed through the expression

$$E_c = E(\text{Mg}_3\text{X}_2) - 3E(\text{Mg}) - 2E(\text{X}), \quad (1)$$

where  $E(\text{Mg}_3\text{X}_2)$  is the energy per formula of the  $\text{Mg}_3\text{X}_2$  monolayer,  $E(\text{Mg})$  is the energy of an isolated Mg atom, and  $E(\text{X})$  is the energy of an isolated X atom. Formation energy can be used to judge how easy a crystal is to decompose into simple substances of the contained elements, which can also be obtained by the above expression, however, now  $E(\text{Mg})$  is the energy of a Mg atom in hexagonal bulk magnesium and  $E(\text{X})$  is that of an X atom in hexagonal bulk X simple substance. The calculated cohesive energies of  $\text{Mg}_3\text{As}_2$  ( $\text{Mg}_3\text{Sb}_2$ ) are  $-3.06$  ( $-2.65$ ) eV/atom, so their formations are exothermic. The deduced formation energies

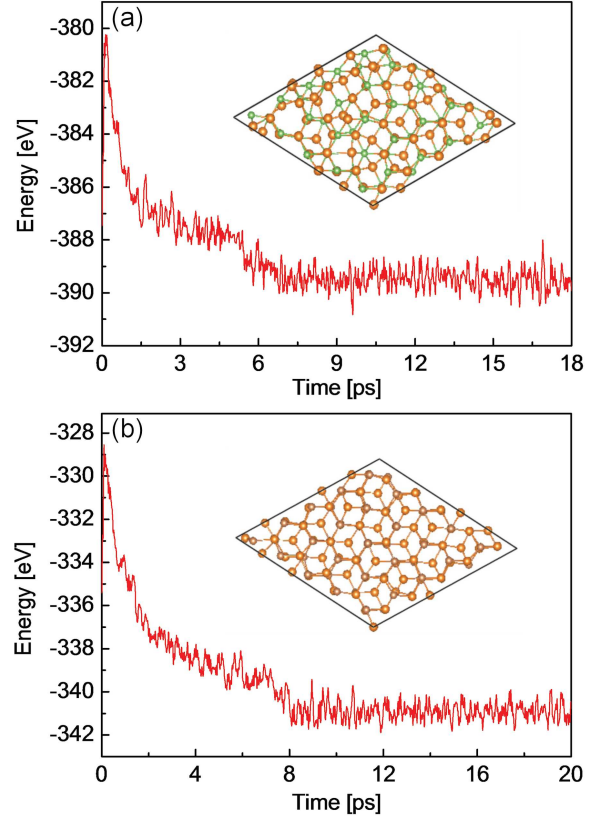


Fig. 3. Changes in the total energy with time of (a)  $\text{Mg}_3\text{As}_2$  and (b)  $\text{Mg}_3\text{Sb}_2$  monolayers at 300 K up to 20 ps. The inserts are the respective crystal structures at 20 ps.

are  $-0.34$  and  $-0.13$  eV/atom, respectively, which means that both monolayers are thermodynamically stable.

The phonon spectra of  $\text{Mg}_3\text{X}_2$  ( $\text{X} = \text{As}, \text{Sb}$ ) monolayers are calculated using a  $6 \times 6 \times 1$  supercell, and the results are presented in Fig. 2. No negative vibrational frequencies are found in the Brillouin zones, thus they are dynamically stable. It is seen that these phonon spectra consist of several parts. The vibrational frequencies decrease, and the acoustic branch with the lowest frequency becomes soft when X changes from As to Sb as a result of the weakening of the interaction between the Mg and X atoms.

Theoretically, the phonon spectrum is obtained without considering temperature (at very low temperature). As the temperature rises, the thermal movement of atoms will enhance. To see the thermal stability of these materials, we performed *ab initio* molecular dynamics simulations using the Nosé-Hoover thermostat [35, 36] in a  $5 \times 5 \times 1$  supercell under 300 K up to 20 ps. The results are illustrated in Fig. 3, which reveals that the structures of these materials are basically intact at the end of the simulation, so they are thermally stable under 300 K.

## 3.2. Electronic properties

The band structures and PDOSs of  $\text{Mg}_3\text{X}_2$  ( $\text{X} = \text{As}, \text{Sb}$ ) monolayers are computed by both the PBE [27] and HSE06 [31] functionals. The results for  $\text{Mg}_3\text{As}_2$  are given in Fig. 4, while those for  $\text{Mg}_3\text{Sb}_2$  are presented in Fig. 5.

Figure 4a shows that both the valence band maximum (VBM) and the conduction band minimum (CBM) of  $\text{Mg}_3\text{As}_2$  are at the  $\Gamma$  point. The band gap computed by the HSE06 functional is 0.44 eV, while that calculated by the PBE functional is about 0 eV. Although there is still no experimental value for it, we think that the former is more reliable according to the work on its bulk counterpart [23]. It is seen that the bands below the Fermi level shift towards the low energy end, whereas those above the Fermi level move upward toward the high energy end when the HSE06 functional is used, which

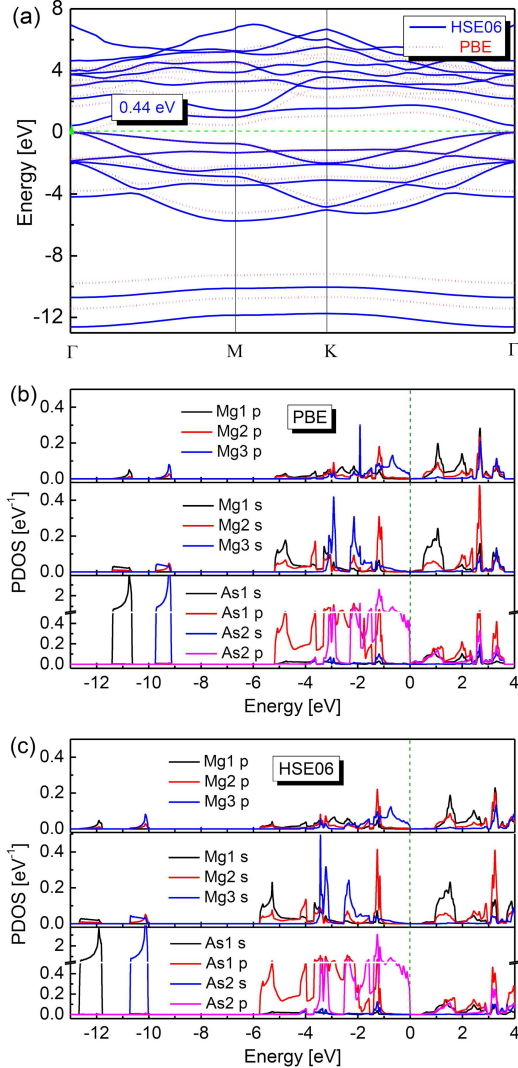


Fig. 4. (a) Band structure and (b–c) PDOSs of  $\text{Mg}_3\text{As}_2$  monolayer obtained by the PBE and the HSE06 functionals.

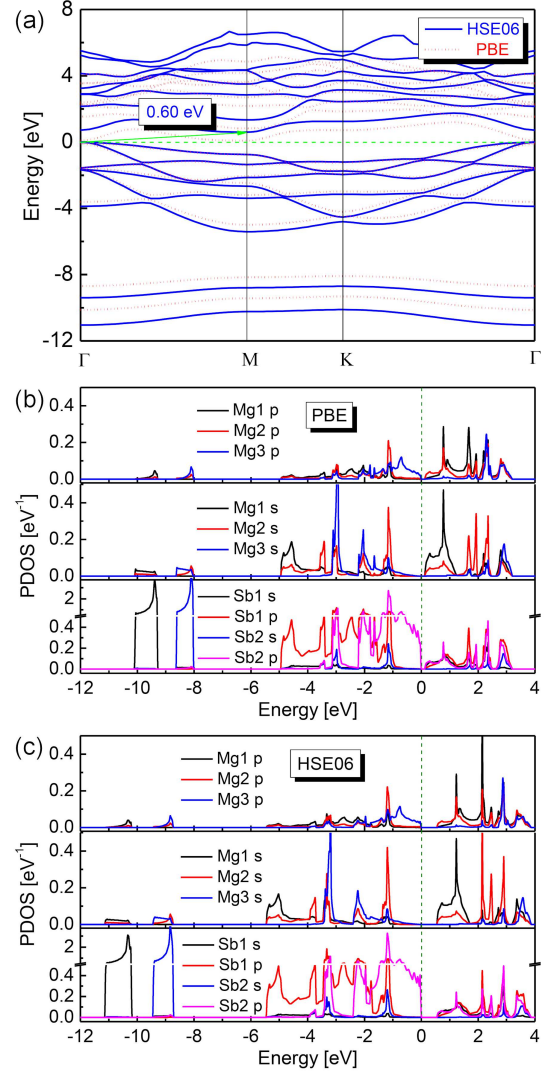


Fig. 5. (a) Band structure and (b–c) PDOSs of  $\text{Mg}_3\text{Sb}_2$  monolayer obtained by the PBE and the HSE06 functionals.

should be caused by the screened Coulomb potential of Hartree–Fock exchange included in this functional [31], finally leading to the emergence of the band gap. To reveal the origin of the bands, we calculated the PDOSs of the constituent atoms of  $\text{Mg}_3\text{As}_2$  by both functionals and presented the results in Fig. 4b and 4c, respectively. The comparison shows that both sets of PDOSs have overall similar profiles, but those below the Fermi level obtained by the HSE06 functional extend and shift to the low energy end, while those above the Fermi level move to the high energy end, as the bands have done. For simplicity, we discuss below only the PDOSs obtained by the HSE06 functional because it is usually thought to be more reliable in describing band structure [23, 32, 33]. One can see in Fig. 4c that the isolated band at about  $-12$  eV comes mainly from the As1  $s$  orbital, the band at around  $-10.5$  eV is mainly from the As2  $s$  orbital,

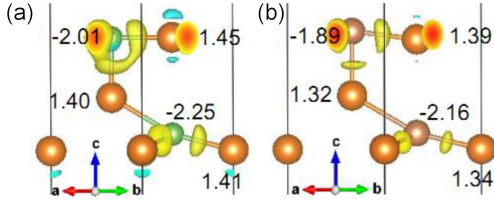


Fig. 6. Calculated electron density differences and Bader charges of (a)  $\text{Mg}_3\text{As}_2$  and (b)  $\text{Mg}_3\text{Sb}_2$  monolayers. Isosurface value:  $0.05 e/\text{\AA}^3$ .

the bands between  $-6$  and  $-4$  eV are mostly formed by the  $p$  orbital of As1 and the  $s$  orbitals of the bonded Mg1 and Mg2 atoms, the bands in the energy range from  $-4$  to  $-1$  eV are principally formed by the  $p$  orbitals of the As1 and As2 atoms and the bonded Mg2 and Mg3 atoms, and the bands between  $-1$  eV and the Fermi level are contributed by the  $p$  orbital of As2 atom and the  $p$  orbital of the bonded Mg3 atom. The bands between the Fermi level and  $3$  eV come from the orbitals of all atoms except the As2  $s$  orbital and the Mg3  $s$  and  $p$  orbitals, and those above  $3$  eV are caused by the  $s$  and  $p$  orbitals of all atoms.

Figure 5a shows that the VBM of  $\text{Mg}_3\text{Sb}_2$  is located at the  $\Gamma$  point, but CBM is at the M point. The band gap obtained by the HSE06 (PBE) functional is  $0.60$  ( $0.17$ ) eV, so  $\text{Mg}_3\text{Sb}_2$  is an indirect narrow band gap semiconductor. The PDOSs of  $\text{Mg}_3\text{Sb}_2$  calculated by the PBE functional are given in Fig. 5b, and those gained by the HSE06 functional are presented in Fig. 5c. It can be seen that processes taking place in the band structure and PDOSs of  $\text{Mg}_3\text{Sb}_2$  are similar to those taking place in  $\text{Mg}_3\text{As}_2$  when the HSE06 functional is used, so they are not discussed a second time. However, comparing PDOSs of  $\text{Mg}_3\text{Sb}_2$  with those of  $\text{Mg}_3\text{As}_2$  obtained by the same functional, one can find two differences: (i) that PDOSs below the Fermi level of  $\text{Mg}_3\text{Sb}_2$  overall shift towards the Fermi level compared with those of  $\text{Mg}_3\text{As}_2$ , (ii) that the Mg1 and Mg2 atoms contribute more to the bands at the bottom of the conduction band, which may result in the alteration of the CBM from the  $\Gamma$  point in  $\text{Mg}_3\text{As}_2$  to the M point in  $\text{Mg}_3\text{Sb}_2$ , thus changing the direct to indirect transition of the band gap. The sharp peaks in the above PDOSs hint at the strong ionicity of the materials, as revealed by Zhang et al. [21]. One can also notice that each Mg atom now has a  $p$  orbital, and its  $p$  orbital hybridizes with its  $s$  orbital, which means that the Mg–X bonds are not pure ionic owing to the complicated bonding situation in  $\text{Mg}_3\text{X}_2$ , i.e., the different Mg–X bonds with different lengths and the different coordination states of different Mg atoms.

To investigate the bonding situation within these materials, we computed their Bader charges [37] and electron density differences, as displayed in Fig. 6. The results indicate that the Mg atoms lose most

of their valence electrons when forming  $\text{Mg}_3\text{X}_2$ . The Mg1 and Mg2 atoms lose almost equal number of electrons, while Mg3 loses more. However, X1 always captures more electrons than X2. As X changes from As to Sb, the numbers of both the lost electrons of the Mg atoms and the obtained electrons of the X atoms decrease entirely due to the weakening of the electronegativity of the X atoms. Both calculated electron density differences have a very low value and show electron transfer from the Mg atoms toward the X atoms. All these indicate that these two monolayers are mainly ionic.

### 3.3. Mechanical properties

Elastic constants are important physical quantities for studying the mechanical properties of materials under different forms of infinitesimal stress, which are indicators for mechanical stability and stiffness. Elastic constants can be derived according to the expression

$$C_{ij} = \frac{\partial \tau_i}{\partial \varepsilon_j}, \quad (2)$$

where  $\tau_i$  is the stress resulting from the strain  $\varepsilon_j$  (in Voigt's form). For two-dimensional (2D) crystals having a  $3m$  point group, there are three independent elements in their elastic stiffness tensors [38]:  $C_{11}$ ,  $C_{12}$ , and  $C_{66}$ .

For 2D crystals, the original elastic constants obtained by first-principles-based codes are not well defined owing to the existence of the vacuum layer along the  $c$  axis, so they are often converted to the in-plane ones based on the length of the  $c$  axis. The deduced elastic constants for  $\text{Mg}_3\text{As}_2$  are  $C_{11} = 63.5$  N/m,  $C_{12} = 34.8$  N/m, and  $C_{66} = 14.3$  N/m. For  $\text{Mg}_3\text{Sb}_2$ , the values are  $49.8$ ,  $27.5$ , and  $11.2$  N/m, respectively. The derived elastic constants of these materials fulfill the mechanical stability criteria [39], i.e.,  $C_{66} > 0$  and  $C_{11}C_{22} - C_{12}^2 > 0$ , which implies that they are mechanically stable. From  $\text{Mg}_3\text{As}_2$  to  $\text{Mg}_3\text{Sb}_2$ , all the corresponding elastic constants decrease as a result of the weakened bonding strength. For each  $\text{Mg}_3\text{X}_2$  monolayer,  $C_{11}$  is much higher than  $C_{12}$ , which hints that exerting normal stress along an arbitrary direction in the  $ab$  plane will cause a smaller strain in that direction than in perpendicular directions. Young's modulus  $E$  is defined as the induced stress vs the applied strain along a certain direction, while Poisson's ratio  $\nu$  is defined as the induced traverse strain vs the longitudinal one under normal stress. They can be inferred from the expressions [39]  $E = (C_{11}^2 - C_{12}^2)/C_{11}$  and  $\nu = C_{12}/C_{11}$ , respectively. The derived Young's moduli for  $\text{Mg}_3\text{X}_2$  ( $X = \text{As}$  and  $X = \text{Sb}$ ) are  $44.4$  and  $34.6$  N/m, respectively, which means that  $\text{Mg}_3\text{As}_2$  is most resistant to uniaxial stress. Both deduced Poisson's ratios are about  $0.55$ .

TABLE I

Calculated vibrational eigenfrequencies at the Brillouin zone centers of  $\text{Mg}_3\text{X}_2$  ( $\text{X} = \text{As}, \text{Sb}$ ) monolayers, unit:  $[\text{cm}^{-1}]$ .

|                          | $E$  | $A_1$ | $E$   | $A_1$ | $A_1$ | $E$   | $E$   | $A_1$ |
|--------------------------|------|-------|-------|-------|-------|-------|-------|-------|
| $\text{Mg}_3\text{As}_2$ | 44.3 | 90.4  | 111.7 | 116.6 | 163.9 | 268.9 | 330.8 | 339.4 |
| $\text{Mg}_3\text{Sb}_2$ | 36.7 | 61.3  | 98.6  | 83.0  | 129.8 | 239.5 | 279.0 | 285.6 |

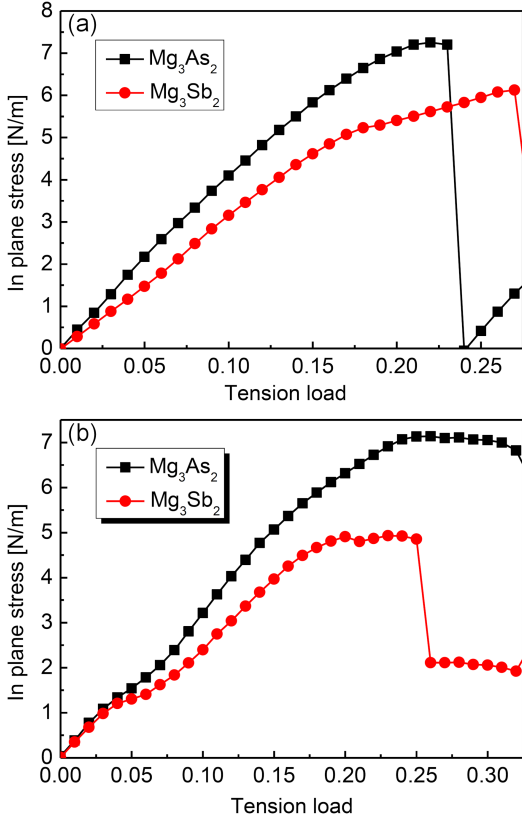


Fig. 7. Calculated strain–stress relations along the (a) zigzag and (b) armchair directions of  $\text{Mg}_3\text{X}_2$  ( $\text{X} = \text{As}, \text{Sb}$ ) monolayers.

Elastic constants only mirror the mechanical response of materials within their elastic limits. To investigate the mechanical properties of  $\text{Mg}_3\text{X}_2$  monolayers at large strains, we calculated their strain–stress relations along the zigzag and armchair directions and presented the results in Fig. 7a and b, respectively. Along the zigzag direction,  $\text{Mg}_3\text{As}_2$  has the highest induced stress, while  $\text{Mg}_3\text{Sb}_2$  can endure the highest strain. The induced stress of  $\text{Mg}_3\text{As}_2$  increases regularly with the applied strain, which reaches 7.26 N/m at the critical strain of 0.22. The As–Mg bonds along this direction are extended from 2.529 to 2.775 Å, accompanied by the break of the As1–Mg2 bonds along the armchair direction. The stress of  $\text{Mg}_3\text{Sb}_2$  first grows linearly with the strain, and then the tendency slows down at the strain of 0.18 until it approaches the critical strain of 0.27, where the corresponding

stress is 6.12 N/m. The Sb2–Mg3 bonds along this direction are stretched from 2.756 to 3.163 Å and then break. The subtle rearrangement of the atoms results in a slightly quicker increase in the lattice constant along the zigzag direction, which leads to the turn of the curve at the strain of 0.18.

Along the armchair direction,  $\text{Mg}_3\text{As}_2$  can withstand a larger critical strain and has a greater maximum stress than  $\text{Mg}_3\text{Sb}_2$ . The behaviors of the strain–stress curves of  $\text{Mg}_3\text{X}_2$  along this direction are more complex, namely, they soften at both the small and the large strain ends before their respective critical points. Investigations indicate that the reason for this is the same as that for the buckling of the strain–stress curve along the zigzag direction of  $\text{Mg}_3\text{Sb}_2$ , so it is not further discussed here. Along the armchair direction, the induced stress of  $\text{Mg}_3\text{As}_2$  hits the maximum value of 7.13 N/m at the critical strain of 0.26. The As2–Mg3 bonds along this direction extend from 2.529 to 2.943 Å, accompanied by their gradual break. The stress of  $\text{Mg}_3\text{Sb}_2$  arrives at its maximum at the strain of 0.23 with a value of 4.93 N/m. The Sb2–Mg3 bonds along this direction elongate from 2.756 to 3.124 Å and then break.

### 3.4. Vibrational and infrared properties

Infrared spectra of crystals are commonly excited by the vibration of the contained atoms at their Brillouin zone centers. There are five atoms in the primitive cell of  $\text{Mg}_3\text{X}_2$  ( $\text{X} = \text{As}, \text{Sb}$ ), which results in fifteen phonon vibrational modes, among which three are acoustic and twelve are optical. According to the analysis from factor group theory, these optical modes can be assigned into the following irreducible groups  $\Gamma_{\text{opt}} = 4A_1(I, R) + 4E(I, R)$ , where  $I$  labels infrared-active modes, while  $R$  labels Raman-active ones. Because  $\text{Mg}_3\text{X}_2$  ( $\text{X} = \text{As}, \text{Sb}$ ) lacks inversion symmetry, all the optical modes are both Raman- and infrared-active. The calculated vibrational eigenfrequencies at the Brillouin zone center are listed in Table I, which reveals that all the values decrease as  $\text{X}$  changes from As to Sb.

To see the origin of these modes, we also computed their eigenvectors. Due to the similarity of the results of  $\text{Mg}_3\text{Sb}_2$ , we only presented the eigenvectors of  $\text{Mg}_3\text{As}_2$  in Fig. 8. It can be seen that: (i) the  $E$  mode with the frequency of 44.3  $\text{cm}^{-1}$  is stimulated by the out-of-phase vibration of the

TABLE II

Calculated Born effective charges  $z_{ii}^*$  [e] and dielectric constants  $\epsilon_{ii}$  of  $\text{Mg}_3\text{X}_2$  (X = As, Sb). Here,  $i = x$  or  $y$ , and “ion” and “ele.” denote the ion and electron contribution, respectively.

|                          |            | Mg1  | Mg2  | Mg3  | X1    | X2    |                 | ion  | ele.  | total |
|--------------------------|------------|------|------|------|-------|-------|-----------------|------|-------|-------|
| $\text{Mg}_3\text{As}_2$ | $z_{xx}^*$ | 2.28 | 1.93 | 1.97 | -3.69 | -2.39 | $\epsilon_{xx}$ | 2.91 | 18.78 | 21.69 |
|                          | $z_{zz}^*$ | 0.16 | 0.19 | 0.20 | -0.25 | -0.30 | $\epsilon_{zz}$ | 0.04 | 1.43  | 1.47  |
| $\text{Mg}_3\text{Sb}_2$ | $z_{xx}^*$ | 2.42 | 2.17 | 1.90 | -4.12 | -2.33 | $\epsilon_{xx}$ | 3.66 | 6.43  | 10.09 |
|                          | $z_{zz}^*$ | 0.16 | 0.14 | 0.13 | -0.24 | -0.19 | $\epsilon_{zz}$ | 0.03 | 1.45  | 1.48  |

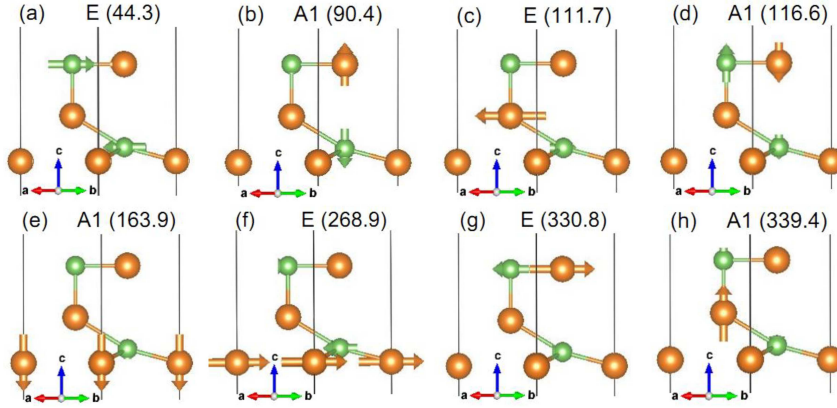


Fig. 8. Vibrational eigenvectors of  $\text{Mg}_3\text{As}_2$  monolayer. The numbers in the parentheses are the corresponding frequencies. Unit:  $[\text{cm}^{-1}]$ .

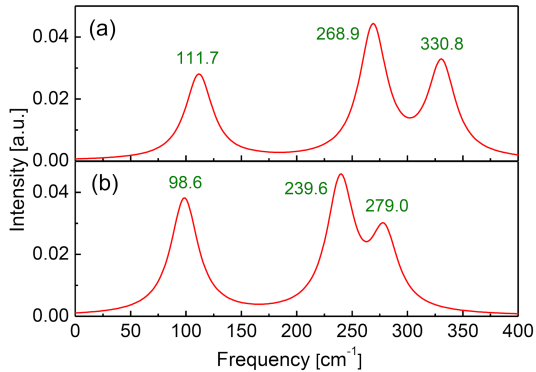


Fig. 9. Simulated infrared spectra of (a)  $\text{Mg}_3\text{As}_2$  and (b)  $\text{Mg}_3\text{Sb}_2$  monolayers. The numbers in the figure are the corresponding frequencies of the peaks. Unit:  $[\text{cm}^{-1}]$ .

two As atoms along the  $(b - a)$  direction in the  $ab$  plane; (ii) the  $A_1$  mode with the frequency of  $90.4 \text{ cm}^{-1}$  is induced by the opposite vibration of the Mg3 and the As1 atoms along the  $c$  axis; (iii) the  $E$  mode with the frequency of  $111.7 \text{ cm}^{-1}$  is excited mainly by the in-plane vibration of the Mg2 atoms; (iv) the  $A_1$  mode with the frequency of  $116.6 \text{ cm}^{-1}$  comes mostly from the out-of-phase vibration of the As2 and the Mg3 atoms along the  $c$  axis; (v) the  $A_1$  mode with the frequency of  $163.9 \text{ cm}^{-1}$  is stimulated by the oscillation of the Mg1 atoms along the  $c$  axis; (vi) the  $E$  mode with

the frequency of  $268.9 \text{ cm}^{-1}$  originates from the out-of-phase movement of the Mg1 and the As1 atoms in the  $ab$  plane; (vii) the  $E$  mode with the frequency of  $330.8 \text{ cm}^{-1}$  is mainly excited by the contrary oscillation of the As2 and the Mg3 atoms along the  $(b - a)$  direction; (viii) the  $A_1$  mode with the frequency of  $339.4 \text{ cm}^{-1}$  is principally induced by the movement of the Mg2 atoms along the  $c$  axis.

The infrared spectra of  $\text{Mg}_3\text{X}_2$  (X = As, Sb) are simulated and displayed in Fig. 9. It is found that the infrared spectra undergo redshift as X changes from As to Sb. Previous analysis reveals that four singly degenerate  $A_1$  modes and four doubly degenerate  $E$  modes exist at the Brillouin zone center for each monolayer, so eight infrared peaks are expected in each simulated infrared spectrum — however, there are only three. To find the reason for this, we have to revise the formula for calculating the infrared spectrum [40]

$$I_m = \sum_{\alpha} \left| \sum_{k,\beta} Z_{k,\alpha\beta}^* U_m(k,\beta) \right|^2, \quad (3)$$

where  $Z_{k,\alpha\beta}^*$  is the Born effective charge (BEC) tensor of the  $k$ -th atom,  $U_m(k,\beta)$  are the vibrational eigenvectors of the atoms for the  $m$ -th infrared mode, and  $\alpha$  and  $\beta$  signify the three components of the cartesian coordinate. For the symmetry of 2D  $\text{Mg}_3\text{X}_2$  (X = As, Sb), the BEC tensor of each constituent atom only has diagonal components, and the value along the  $xx$  direction equals that

along the  $yy$  direction, as presented in Table II. The results uncover that the Mg atoms have positive values while the X atoms have negative ones for their different electronegativities, and the values of the  $xx$  components are much greater than those of their respective  $zz$  components. From the calculated BECs and the eigenvectors shown in Fig. 8, we find that the infrared peaks with high intensity are mainly caused by the large vibrational eigenvectors of the in-plane vibration of the Mg atoms, as shown in Fig. 8c, f, and g. Those with negligible intensity are induced by the small BECs along the  $c$  axis, as displayed in Fig. 8e and h, or by the offset of the summing of the contribution of the out-of-phase vibration in the  $ab$  plane, as shown in Fig. 8a, or by both factors, as presented in Figs. 8(b) and (d).

### 3.5. Piezoelectric and dielectric properties

Piezoelectric materials, semiconductors or insulators without inversion symmetry, can convert stress to electricity or vice versa, so they are often used in sensors and energy harvesting devices [41]. Commonly, there are two types of piezoelectric tensors [42], i.e., piezoelectric stress tensor ( $e_{ik}$ ) and piezoelectric strain tensor ( $d_{ik}$ ), which are connected by elastic stiffness tensor ( $C_{ij}$ ) via the relation  $e_{ik} = d_{ij}C_{jk}$ . The former is defined as

$$e_{ik} = \left( \frac{\partial P_i}{\partial \varepsilon_k} \right)_E, \quad (4)$$

where  $P_i$  is the polarization along the  $i$  direction induced by the  $k$  component of strain  $\varepsilon$  without an electric field. As for a 2D crystal of the  $3m$  point group, there are two independent elements in its piezoelectric stress tensor,  $e_{11}$  and  $e_{31}$ . The latter is defined as

$$d_{ik} = \left( \frac{\partial P_i}{\partial \tau_k} \right)_E, \quad (5)$$

i.e., polarization component  $P_i$  caused by the stress component  $\tau_k$  under zero electric field. In the case of  $\text{Mg}_3\text{X}_2$  ( $\text{X} = \text{As}, \text{Sb}$ ), the independent elements are  $d_{11}$  and  $d_{31}$ . The ultimate relation between these two sets of piezoelectric coefficients is  $d_{11} = e_{11}/(C_{11} - C_{12})$  and  $d_{31} = e_{31}/(C_{11} + C_{12})$ . As for 2D materials,  $e_{31}$  and  $d_{31}$  are too small to mention, so they are often omitted. The computed piezoelectric coefficients for  $\text{Mg}_3\text{As}_2$  are  $e_{11} = -594.2$  pC/m and  $d_{11} = -20.7$  pm/V. For  $\text{Mg}_3\text{Sb}_2$ , the results are  $e_{11} = -540.2$  pC/m and  $d_{11} = -24.2$  pm/V. These piezoelectric stress coefficients  $e_{11}$  are much larger than for  $\text{MoS}_2$  (290 pC/m) [43] and for  $\text{AlN}$  (220.5 pC/m) [44]. The calculations also reveal that the piezoelectric stress coefficients are mostly contributed by the ions due to the ionic characteristics of these materials.

Dielectric constants reflect the response of materials under an electric field, which can also be divided into ion contribution and electron

contribution. For  $\text{Mg}_3\text{As}_2$  ( $\text{Mg}_3\text{Sb}_2$ ) monolayer, the ion contributions are  $\varepsilon_{xx}^i = \varepsilon_{zz}^i = 2.91$  (3.66) and  $\varepsilon_{zz}^i = 0.04$  (0.03), while the electron contributions are  $\varepsilon_{xx}^e = \varepsilon_{zz}^e = 18.78$  (6.43) and  $\varepsilon_{zz}^e = 1.43$  (1.45), so the total is  $\varepsilon_{xx} = \varepsilon_{zz} = 21.69$  (10.09) and  $\varepsilon_{zz} = 1.47$  (1.48), as shown in Table II. It is found that electrons have the largest contribution to the total dielectric constants, but their contribution declines from  $\text{Mg}_3\text{As}_2$  to  $\text{Mg}_3\text{Sb}_2$ .

## 4. Conclusions

In this work, the electronic, mechanical, vibrational, and piezoelectric properties of  $\text{Mg}_3\text{X}_2$  ( $\text{X} = \text{As}, \text{Sb}$ ) monolayers were studied by first-principles calculations. The derived formation energies, phonon spectra, and elastic constants reveal, respectively, the thermodynamical, dynamical, and mechanical stability of 2D  $\text{Mg}_3\text{X}_2$  ( $\text{X} = \text{As}, \text{Sb}$ ). Calculations indicate that  $\text{Mg}_3\text{As}_2$  ( $\text{Mg}_3\text{Sb}_2$ ) is a direct (an indirect) band gap semiconductor with a gap of 0.44 (0.60) eV at the HSE06 level. For each monolayer, the top of the valance band is formed by the  $p$  orbitals of the X2 and the Mg3 atoms, while the Mg3 atom and the X  $s$  orbitals have almost no contribution to the bottom of the conduction band. Strong peaks in the calculated PDOSs hint at the ionicity of the studied systems, which is confirmed by the Bader charge analysis. In the zigzag (armchair) direction,  $\text{Mg}_3\text{As}_2$  has a higher strength of about 7.26 (7.13) N/m at strain 0.22 (0.26) than  $\text{Mg}_3\text{Sb}_2$ , which has a strength of 6.12 (4.93) N/m at strain 0.27 (0.23). However, the change in the strain-stress curves in the armchair direction is not as regular as that along the zigzag direction because of the subtle difference in the adjustment of the atomic sites under the applied strains along these two directions. Eight infrared peaks are predicted, while only three appear in the simulated infrared vibrational spectra. Further studies reveal that the vanishment of the  $A_1$  modes is caused by the small BECs of the constituent atoms along the  $c$  axis, while the disappearance of the  $E$  modes is induced by the offset of the summing of the contribution of the out-of-phase vibration in the  $ab$  plane. The calculated piezoelectric stress coefficient of  $\text{Mg}_3\text{As}_2$  ( $\text{Mg}_3\text{Sb}_2$ ) is  $-594.2$  ( $-540.2$ ) pC/m, indicating their possible application in the field of piezoelectric electronics.

## Acknowledgments

This work was supported by the Natural Science Youth Foundation of Henan Province, China, under Grant No. 232300421350, and the Science and Technology Research Project of Henan Province, China, under Grant No. 232103810034.

## References

- [1] L.M. Watson, C.A.W. Marshall, C.P. Cardoso, *J. Phys. F Met. Phys.* **14**, 113 (1984).
- [2] A.A. Nayeb-Hashemi, J.B. Clark, *Bull. Alloy Phase Diagr.* **6**, 432 (1985).
- [3] K. Pigon, *Helv. Phys. Acta* **41**, 1104 (1968).
- [4] K. Yang, J. Shi, S. Ding, R. Su, W. Cui, M. Xu, J. Hao, Y. Li, *RSC Adv.* **9**, 34401 (2019).
- [5] Y. Imai, A. Watanabe, *J. Mater. Sci.* **41**, 2435 (2006).
- [6] S. Ding, R. Su, W. Cui, J. Hao, J. Shi, Y. Li, *ACS Omega* **5**, 31902 (2020).
- [7] M. Calderón-Cueva, W. Peng, S.M. Clarke et al., *Chem. Mater.* **33**, 567 (2021).
- [8] S. Ohno, K. Imasato, S. Anand et al., *Joule* **2**, 141 (2018).
- [9] C.L. Condrón, S.M. Kauzlarich, F. Gascoin, G.J. Snyder, *J. Solid State Chem.* **179**, 2252 (2006).
- [10] A. Bhardwaj, A. Rajput, A.K. Shukla et al., *RSC Adv.* **3**, 8504 (2013).
- [11] Z. Ren, J. Shuai, J. Mao, Q. Zhu, S. Song, Y. Ni, S. Chen, *Acta Mater.* **143**, 265 (2018).
- [12] Z. Liu, W. Gao, H. Oshima, K. Nagase, C.H. Lee, T. Mori, *Nat. Commun.* **13**, 1120 (2022).
- [13] B. Xu, R. Li, G. Yu, S. Ma, Y. Wang, Y. Wang, L. Yi, *J. Phys. Soc. Jpn.* **86**, 024601 (2017).
- [14] J. Li, S. Zheng, T. Fang, L. Yue, S. Zhang, G. Lu, *Phys. Chem. Chem. Phys.* **20**, 7686 (2018).
- [15] X. Sun, X. Li, J. Yang et al., *J. Comput. Chem.* **40**, 1693 (2019).
- [16] J. Zhang, B.B. Iversen, *J. Appl. Phys.* **126**, 085104 (2019).
- [17] C. Xia, J. Cui, Y. Chen, *ACS Appl. Electron. Mater.* **2**, 2745 (2020).
- [18] X. Wang, Y. Lu, Z. Hu, X. Shao, *Metals* **11**, 971 (2021).
- [19] J. Tani, M. Takahashi, H. Kido, *Physica B* **405**, 4219 (2010).
- [20] M. Ullah, G. Murtaza, A. Mahmood, S.M. Ramay, *Mater. Res. Bull.* **91**, 22 (2017).
- [21] J. Zhang, L. Song, M. Sist, K. Tolborg, B.B. Iversen, *Nat. Commu.* **9**, 4716 (2018).
- [22] Q. Peng, S. Zhao, X. Yuan, X.J. Chen, *Materials* **15**, 7161 (2022).
- [23] Z.L. Lv, G. Liu, X.F. Wang, H.L. Cui, *Mater. Today Commu.* **37**, 107511 (2023).
- [24] S. Huang, Z. Wang, R. Xiong, H. Yu, J. Shi, *Nano Energy* **62**, 212 (2019).
- [25] Z. Chang, J. Ma, K. Yuan et al., *Front. Mech. Eng.* **8**, 876655 (2022).
- [26] G. Kresse, J. Furthmüller, *Phys. Rev. B* **54**, 11169 (1996).
- [27] J.P. Perdew, K. Burke, M. Ernzerhof, *Phys. Rev. Lett.* **77**, 3865 (1996).
- [28] G. Kresse, D. Joubert, *Phys. Rev. B* **59**, 1758 (1999).
- [29] H.J. Monkhorst, J.D. Pack, *Phys. Rev. B* **13**, 5188 (1976).
- [30] A. Togo, F. Oba, I. Tanaka, *Phys. Rev. B* **78**, 134106 (2008).
- [31] J. Heyd, G.E. Scuseria, M. Ernzerhof, *J. Chem. Phys.* **118**, 8207 (2003).
- [32] C. Zhang, D.D. Pang, X.Q. Huang, H.Y. Xue, Z.L. Lv, H.L. Cui, *Acta Phys. Pol. A* **134**, 1163 (2018).
- [33] Z.Q. Zhen, H.Y. Wang, *Acta Phys. Pol. A* **137**, 1095 (2020).
- [34] R. Juza, R. Kroebel, *Z. Anorg. Allg. Chem.* **331**, 187 (1964).
- [35] S. Nosé, *J. Chem. Phys.* **81**, 511 (1984).
- [36] W.G. Hoover, *Phys. Rev. A* **31**, 1695 (1985).
- [37] R.F.W. Bader, *Atoms in Molecules: A Quantum Theory*, Clarendon Press, Oxford, 1990.
- [38] L. Dong, J. Lou, V.B. Shenoy, *ACS Nano* **11**, 8242 (2017).
- [39] Y. Ding, Y. Wang, *J. Phys. Chem. C* **117**, 18266 (2013).
- [40] P. Giannozzi, S. Baroni, *J. Chem. Phys.* **100**, 8537 (1994).
- [41] R. Fei, W. Li, J. Li, L. Yang, *Appl. Phys. Lett.* **107**, 173104 (2015).
- [42] M. Catti, Y. Noel, R. Dovesi, *J. Phys. Chem. Solids* **64**, 2183 (2003).
- [43] H. Zhu, Y. Wang, J. Xiao, et al., *Nat. Nanotechnol.* **10**, 151 (2015).
- [44] S.J. Lv, G.X. Yin, H.L. Cui, H.Y. Wang, *Phys. Status Solidi B* **258**, 2100216 (2021).